Heliyon 10 (2024) e23840

Contents lists available at ScienceDirect

Heliyon

journal homepage: www.cell.com/heliyon

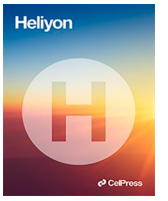

Review article

# Physiochemical characterization of metal organic framework materials: A mini review

Hussein Rasool Abid [a,b,*], Muhammad Rizwan Azhar [c,**], Stefan Iglauer [a], Zana Hassan Rada [a], Ahmed Al-Yaseri [d], Alireza Keshavarz [a]

[a] Energy and Resource Discipline, School of Engineering, Edith Cowan University, Joondalup, WA 6027, Australia
[b] Environmental Health Department, Applied Medical Sciences, University of Kerbala, Karbala 56001, Iraq
[c] Chemical Engineering Discipline, School of Engineering, Edith Cowan University, Joondalup, WA
[d] College of Petroleum Engineering and Geoscience, King Fahd University of Petroleum and Minerals, Saudi Arabia

ARTICLE INFO

*Keywords:*
metal organic framework (MOF)
Characterization
X-ray diffraction
Thermo-gravimetric analysis
surface area
Infrared spectroscopy

ABSTRACT

Metal-organic frameworks (MOFs) are promising materials offering exceptional performance across a myriad of applications, attributable to their remarkable physicochemical properties such as regular porosity, crystalline structure, and tailored functional groups. Despite their potential, there is a lack of dedicated reviews that focus on key physicochemical characterizations of MOFs for the beginners and new researchers in the field. This review is written based on our expertise in the synthesis and characterization of MOFs, specifically to provide a right direction for the researcher who is a beginner in this area. In this way, experimental errors can be reduced, and wastage of time and chemicals can be avoided when new researchers conduct a study. In this article, this topic is critically analyzed, and findings and conclusions are presented. We reviewed three well-known XRD techniques, including PXRD, single crystal XRD, and SAXS, which were used for XRD analysis depending on the crystal size and the quality of crystal morphology. The TGA profile was an effective factor for evaluating the quality of the activation process and for ensuring the successful investigation for other characterizations. The BET and pore size were significantly affected by the activation process and selective benzene chain cross-linkers. FTIR is a prominent method that is used to investigate the functional groups on pore surfaces, and this method is successfully used to evaluate the activation process, characterize functionalized MOFs, and estimate their applications. The most significant methods of characterization include the X-ray diffraction, which is utilized for structural identification, and thermogravimetric analysis (TGA), which is used for exploring thermal decomposition. It is important to note that the thermal stability of MOFs is influenced by two main factors: the metal-ligand interaction and the type of functional groups attached to the organic ligand. The textural properties of the MOFs, on the other hand, can be scrutinized through nitrogen adsorption-desorption isotherms experiments at 77 K. However, for smaller pore size, the Argon adsorption-desorption isotherm at 87.3 K is preferred. Furthermore, the $CO_2$ adsorption isotherm at 273 K can be used to measure ultra-micropore sizes and sizes lower than these, which cannot be measured by using the $N_2$ adsorption-desorption isotherm at 77 K. The highest BET was observed in high-valence MOFs that are constructed based on the metal-oxo cluster, which has an excellent ability to control their textural properties. It was found that the synthesis procedure (including the choice of solvent,

* Corresponding author: Energy and Resource Discipline, School of Engineering, Edith Cowan University, Joondalup, WA 6027, Australia.
** Corresponding author: Chemical Engineering Discipline, School of Engineering, Edith Cowan University, Joondalup, WA 6027, Australia.
*E-mail addresses:* hussein.r@uokerbala.edu.iq (H.R. Abid), m.azhar@ecu.edu.au (M.R. Azhar).

https://doi.org/10.1016/j.heliyon.2023.e23840
Received 23 August 2023; Received in revised form 30 November 2023; Accepted 13 December 2023
Available online 16 December 2023

cross-linker, secondary metal, surface functional groups, and temperature), activation method, and pressure significantly impact the surface area of the MOF and, by extension, its structural integrity. Additionally, Fourier-transform infrared spectroscopy plays a crucial role in identifying active MOF functional groups. Understanding these physicochemical properties and utilizing relevant characterization techniques will enable more precise MOF selection for specific applications.

## 1. Introduction

Metal-organic frameworks (MOFs) or coordination polymers (CPS) are highly ordered porous hybrid materials, formed through the coordination of an organic linker with secondary building units (SBU) or clusters enriched with a coordinated anion [1]. Among the coordinated anions, oxygen is prevalent. Lately, sulfur-based MOFs and CPs have been prepared using sulfur as the coordinated anion in SBU, and these materials have attracted attention as exceptional crystalline materials [2]. Several researchers working in different research areas are interested in MOFs owing to their high specific surface area (up to 7000 $m^2/g$), tunable pore size and functionalities, high flexibility, various unique morphologies, high porosity (free space of up to 90 %), and an excellent thermal/chemical stability [3]. To date, MOFs have found diverse applications, including gas storage and separation [4], catalysis [5], sensing [6,7] and drug delivery [8]. However, to broaden the scope of MOF utilization, it is crucial to adhere to appropriate synthesis, activation, and characterization techniques. Currently, several synthesis procedures are employed to prepare a myriad of MOFs, such as solvothermal/hydrothermal, microwave, ultrasonic, ionothermal synthesis, and electrochemical methods [9,10]. Moreover, MOFs are activated—a process to remove undesirable guest molecules and unblock pores—via methods like direct heating, solvent exchange followed by heating, supercritical $CO_2$ drying, benzene freeze-drying, and photothermal activation [10]. This results in a diverse range of characteristics, even when using the same metal and organic ligands.

Given the rapid development of MOFs and their expanding list of applications, the need for accurate physicochemical and electrochemical characterizations to unravel their structural integrity, thermodynamic stability, and functional properties is paramount. Numerous studies have reported detailed insights into the synthesis, activation, and modification of MOFs [11]. However, it is extremely important to provide a consolidated review on distinct characterization techniques to elucidate successful synthesis, doping of heteroatoms for tailored properties, and further calcination or carbonization for achieving thermodynamic stability, electronic conductivity, and ionic conductivity [12,13]. Moreover, the swift advancement of MOFs has led to the development of prototypes and devices for various applications. Yet, for having application in diverse fields, MOFs need to be synthesized in the form of bulk powders, thin films, and other forms, necessitating robust and authentic characterization techniques to achieve the desired properties [14]. Several reviews have discussed the applications of MOFs. For instance, MOFs have been widely used as carriers for drugs in pharmaceutical applications due to their nanoscale size and effective tunable functionalities [15]. In addition, MOFs have been used as smart nanomaterials for biomedical applications and medical therapy [16–18]. Furthermore, MOFs were utilized for gas and energy storage [19]. Greenhouse gases were effectively stored in most MOFs used by researchers since MOFs have a huge surface and large pore volume. Recently, MOFs have been widely investigated to store energy via hydrogen storage [20]. Also, smart sensors have been successfully prepared based on selective characteristics of MOFs [21]. Functionalized MOFs have increasingly been used to fabricate sensors for various purposes depending on the chemical characteristics of their functional groups. MOFs are proved to be superior when compared with other sensing materials owing to their distinguished sensing properties [22]. MOFs have been introduced as ideal candidates for heterogeneous catalysis for reactions owing to (i) their physicochemical properties, (ii) the porous hybrid metal/organic assemblies, and (iii) the existence of vacant metal sites and reachable organic moieties [23]. MOF-derived materials draw considerable research interest as catalysts for organic reactions owing to their flexible tunability, high catalytic activity, and high controllability in the fabrication of a catalyst structure [24]. Therefore, to utilize MOFs in all these applications, the appropriate fabrication and characterization of MOFs is necessary.

In this review, we have assessed the key MOFs that have been widely utilized in the past two decades. This work provides a swift screening analysis of the principal MOFs, imparts a fundamental understanding of MOFs in general, and serves as a gateway for newcomers to this research field. Our review, grounded in extensive personal hands-on experience, observations, and literature analysis, will benefit new researchers in the field of MOFs synthesis, characterization, and applications. Furthermore, it provides outlooks and future directions on the selection of specific characterization techniques for existing and emerging MOFs.

## 2. MOFs characterization

### 2.1. XRD analysis

X-ray facilities include a group of spectroscopic techniques of considerable importance. These facilities technically operate with optical methods, and therefore, they are accordingly classified based on the interaction of X-rays with matter i.e., absorption, refraction/reflection, and scattering of X-rays [25]. Furthermore, three sub-categories of X-ray techniques exist, i.e., X-ray fluorescence (XRF) spectrometry, proton-induced X-ray emission (PIXE) spectrometry, and X-ray diffraction (XRD). XRF and PIXE are usually used for elemental analysis, while XRD is mainly used to identify the fingerprint of crystalline materials [26] as well as its morphology [27]. Crystalline materials are made of atoms with a highly ordered arrangement in a three-dimensional space. The symmetrical crystal

structure of these materials is built based on repeating units, which are referred to as unit cells. The sizes and shapes of these unit cells control the directions of constructive interference [28]. MOFs are highly ordered crystalline porous materials. Therefore, XRD is a more helpful technique to characterize MOFs as compared to other techniques. Specifically, in case of characterization of unknown materials, X-ray diffraction (XRD) analysis is preferred because it can provide important information on the structures of materials [12]. MOFs are polymetric and engineering materials with a high degree of crystallinity; thus, each MOF has its unique structure [9]. Therefore, XRD analysis should be performed as the first characterization to identify the synthesized materials and their purities prior to performing further investigations. The two targets for XRD analysis are the determination of a new crystal structure and confirmation of existing crystal structures. The details are provided in the following sections.

Generally, MOFs can be characterized through single-crystal X-ray diffraction (SCXRD) analysis. Single-crystal X-ray crystallography (or, more commonly, SCXRD) analyses the atomic arrangement in a single crystal using an X-ray beam and a diffractometer. The SCXRD data can determine and refine the new crystalline structure of an unknown material. In addition, this data is required to know the stability of the crystals in operating conditions. Crystals might be sensitive to visible light, atmospheric air, or moisture content. Therefore, a pre-treatment of the crystals is necessary before analysis. For instance, the sample can be mounted inside sealed thin-wall glass capillary tubes in an inert environment [29,30].

However, SCXRD requires a perfect crystal having a large size (>100 μm) [25,31]. For instance, Zeolitic imidazolate frameworks (ZIF)-67 (Zn) is usually synthesized with large uniform crystals [32] as shown in Fig. 1a. However, some large crystals cannot be analyzed by single crystal XRD, because they might not be high quality crystals (e.g., compare MIL-53 (Al) (Material Institute Lavoisier) in Fig. 1b) that are not suitable for single crystal XRD. To resolve this, alternatively, their structure is computationally resolved using the data of powder X-ray diffractometers (PXRD) [4,33,34]. Practically, micro-size crystals are represented by the patterns of sharp and narrow peaks, whereas the patterns of wide and short peaks are associated with nano-sized crystals.

Some MOFs such as Zr-BPDC (biphenyl dicarboxylic acid-BPDC) are hydrothermally synthesized using benzoic acid as a modulator. Benzoic acid modifies the crystal size of Zr-BPDC from nanoscale to micro-scale as shown in the SEM images of Fig. 2. This trend is confirmed by the XRD pattern, where the peaks become narrower with an increase in the amount of benzoic acid. PXRD instruments are supplied with sample holders and detectors attached to goniometers; the sample holder is rotated to the correct position at a specified angle with the location of the detector to ensure that the reflected rays are captured and detected by the detector [36]. This methodology is classified under reflection geometry. Conversely, an alternative approach in PXRD utilizes transmission geometry. Both techniques have been used for structural analysis of materials. A high-resolution PXRD in combination with computational analysis is widely used to determine MOF structures [37,38]. It should be noted that the selection of a helpful XRD technique to determine structures depends on the crystal size of the MOF and the quality of its morphology. For PXRD, the sample should be in the form of a fine homogenous powder of a crystallite size ranging from 0.1 to 1 μm. Based on the target of the experiment and availability of the instrument, the crystal sizes might not be comprehensively depended. Specifically, when quantitative analysis is not required, PXRD can be used for analysing a higher crystalline size (30 μm) or lower crystalline size (<0.1 μ) [30,39,40].

In addition, PXRD can measure defects in the texture or strain of crystals and identify mineral phases; however, PXRD only offers the average information of a bulk number of grains or crystallites targeted by the X-ray beam [37]. Furthermore, the average crystal size of small crystalline particles (<100 nm) can be determined via the Scherrer equation.

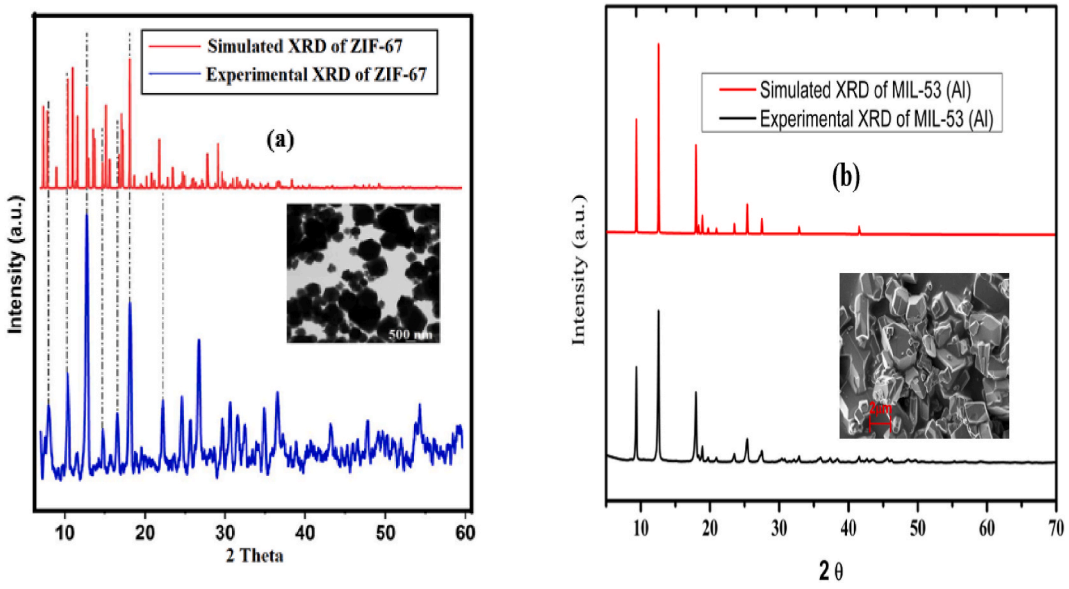


**Fig. 1.** XRD pattern and morphological image (SEM Image) of (a) ZIF-67 [35] and (b) MIL-53(Al).

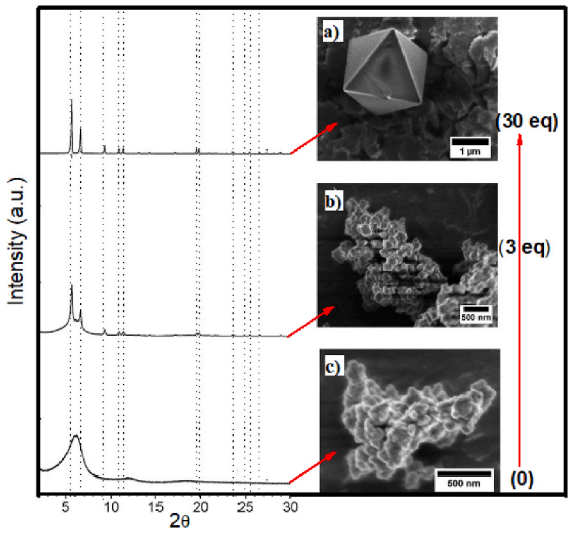


**Fig. 2.** Powder XRD patterns and SEM images of Zr- MOF using benzoic acid as the modulator in different equivalent amount, a) 30, b) 3 and c) 0 [41].

$$D = \frac{K\lambda}{W cos\theta} \tag{1}$$

where D is the mean crystal size, W is the full-width at half of the maximum reflection, K is a shape factor that typically has a value between 0.89 and 0.94 [42]. λ is the wavelength that usually depends on the X-ray diffractometers, and Θ is the scattering angle [43]. The structural identity of extremely small crystals (<10 nm) can be examined via small-angle X-ray scattering (SAXS). SAXS is a dependent technique for determining the structural properties of samples at resolutions between 1 nm and 1000 nm [44]. SAXS can help researchers in understanding morphology at nanometer and angstrom length scales using complementary small angle X-ray scattering. Correlation functions are used to determine the crystal size, particle size distribution, crystal shape, and organization into hierarchical structures [45]. SAXS differs from conventional X-ray diffraction because in case of SAXS, a collimated X-ray beam interacts with particles that have much larger dimensions than the wavelength of the radiation. Thus, the detected scattering angles are located in a narrow region from 0.1° to 10° [46]. The precision of the results (e.g., pore structure) is affected by the experimental technique used and the quality of the sample [47]. In a typical SAXS experiment, the sample is mounted in transmission, and the scattered X-ray radiation is collected by an area detector [48–50].

**Table 1**
Advantages and limitations of essential XRD techniques.

| Instrument | Advantages | Limitation |
|---|---|---|
| 1 Powder X-ray diffraction (PXRD) | 1 Successful nondestructive measurement is guaranteed.<br>2 The phase analysis is used to distinct between amorphous and crystalline materials (with possibilities of microstructural characterization and refinement and solution of crystalline structures),<br>3 XRPD data can be used for wide range measurements such as:<br>(i) Qualitative analyses (phase compositions) and quantitative analyses (phase abundances),<br>(ii) Bravais lattice symmetry and lattice parameters,<br>(iii) Residual strain (macrostrain),<br>(iv) Crystal structure,<br>(v) Crystallite size and microstrain [30,40]. | 1 Isostructurality challenge if phases have similar crystalline structures and XRD patterns although they are chemically completely different.<br>2 Amorphous phases cannot be identified.<br>3 It is hard to identify or analyze minor phases.<br>4 Long procedure and sometimes, it is very difficult to calculate the Phase quantification [30,40]. |
| 2 Single crystal X-ray (SCXR) | 1 The primary goal of single-crystal x-ray diffraction is to determine crystal structure and the arrangement of atoms in a unit cell.<br>2 From single-crystal XRD data it is possible to solve and refine the crystalline materials [29,30]. | 1- Must have a single, robust (stable) crystal, generally >100 µm in size, obviously seen as a single crystal.<br>2- Long time required for data collection commonly needs between 24 and 72 h [29,30]. |
| 3 small-angle X-ray scattering (SAXS). | 1 SAXS often needs very little time for sample preparation.<br>2 It has typical advantages over other techniques such as electron microscope instruments.<br>3 it can determine nanoparticle size distributions, resolve the size and shape of (monodisperse) macromolecules, determine pore sizes, characteristic distances of partially ordered materials [51,52]. | 1 Their properties are size-dependent.<br>2 when all nanoparticles are not identical, it only provides the average size of a population of nanoparticles in the specimen.<br>3 The final recorded pattern is essentially an integrated superposition (a self-convolution) of many adjacent pinhole patterns [51,52]. |

The PXRD instrument is commonly used for wide-angle X-ray scattering to identify a large crystal structure (>100 nm), while SAXS identifies a nanoparticle structure (<10 nm). Table 1 depicts further significant differences between the abovementioned prominent XRD techniques.

Different crystalline structures of organic compounds, inorganic-organic frameworks, and mineral species can be identified by comparing the positions of the various experimental diffraction peaks with those in the published literature [53]. However, occasionally, a shift in the peaks might be observed, a phenomenon which can identify internal stresses, twin boundaries, stacking faults, chemical heterogeneities, a small crystal size, or structural defects [54,55]. Table 2 illustrates various MOFs that were analyzed by using different techniques based on their crystal sizes.

### 2.2. Thermogravimetric analysis (TGA)

TGA is usually used to determine thermal or oxidative stability, chemical composition, expected lifetime, rate of decomposition, the influence of the surrounding environment on thermal stability, or the moisture and volatiles content [74]. In TGA, the amount and the rate of weight change of the sample is measured as a function of temperature and/or time in a controlled atmosphere. TGA profiles are initially obtained for newly synthesized MOFs (before activation) to identify the types of contaminants, non-reacted precursors, and decomposition temperatures [55]; This information is used to determine suitable activation process temperatures. Subsequently, TGA is repeated for the activated MOFs to test the performance of the activation process. Thermal MOF stability depends on two factors, namely metal-ligand interaction, and the functional groups on the organic ligand–note that high valence metals and high multidentate ligands generate a high thermal MOF stability. Mainly, the metal and organic linkers are connected together through coordination bonds via nodes, which might be metals or metal-oxo clusters. Therefore, the number of superficial functional groups, degree of crystallinity, and density of metal-oxo clusters positively affect the clusters-linking density of the final extended MOFs, accordingly affecting their thermal stabilities. MOFs that have a stable framework structure built by highly connected metal-oxo cluster nodes and organic linkers can demonstrate immense potential in gas storage, adsorption, and separation [75,76]. Specifically, the interactions between the oxygen atom in the carbonyl group of the deprotonated organic linker and the metal atom of the metal node should be sufficiently strong. The strength of this bond is dominated by the coordination number of the metal atoms and the specific coordination geometry. High coordination numbers have been shown to have high thermal stability [77,78]. For instance, MIL-53(Al) contains a trivalent metal and benzene dicarboxylic acid (BDC), and the free BDC molecules were completely eliminated through the activation process, while the integrity of the structure could be maintained up to 803 K. Besides, using a dicarboxylic aliphatic linker instead of an aromatic linker causes the MOF to have a low thermal stability, which is observed in the case of MOF-801 (which decomposes at 548 K [79]). The lowest thermal stability among MOFs was detected in Mn-BTT, which decomposes at 473 K (Table 3) due to the use of nitrogen donor ligands, which are strongly coordinated with solvent molecules (dimethyl formamide, (DMF)). Therefore, its structure is destroyed upon removal of DMF molecules. However, coordination of a soft ligand containing nitrogen and soft metal enhances the thermal MOF stability (such as in case of $Zn_3(BTP)_2$, which exhibits a high thermal stability up to 723 K owing to strong linkage between the pyrazolate-based linker and the low valence metal when using methanol to exchange DMF during the activation process at room temperature [80]). Nevertheless, active functional groups on organic ligands decrease the thermal MOF stability because the functional group can affect the charge distribution and electronegativity of the whole MOF structure. As a result, the bond strength between the metal and oxygen decreases. Functional groups that are enriched with free electrons can reduce the thermal and chemical stability of the MOFs without a doubt. In this regard, ZIF has methyl groups which are not enriched with free electrons. These methyl

**Table 2**
XRD analysis results for various MOFs.

| MOF | Crystal Size | XRD Technique | Structural Formula | Reference |
|---|---|---|---|---|
| MIL-96 (Al) | 0.04 × 0.04 × 0.04 ($mm^3$) | Single-crystal X-ray | $Al_{12}O(OH)18(H_2O)_3(Al_2(OH)_4)$ [btc]6·24$H_2O$ | [56] |
| MOF-5 | 0.1 × 0.1 × 0.18 ($mm^3$) | Single-crystal X-ray | $Zn_4O(BDC)_3$·$(DMF)_8(C_6H_5Cl)$ | [57] |
| UiO-66(Zr) | 2 × 2 × 2 ($\mu m^3$) | PXRD | $Zr_{24}$ $O_{120}$ $C_{192}$ $H_{96}$ | [58] |
| MOF-892 | 0.14 × 0.09 × 0.08 ($mm^3$) | Single-crystal X-ray | $Zr_6O_4(OH)_4(CH_3CO_2)_6(CO_2)_6$ | [59] |
| CPO-27-Co | 0.02 × 0.02 × 0.20 ($mm^3$) | Single-crystal X-ray | $[Co_2(C_8H_2O_6)$ $(H_2O)_2]$·$8H_2O$ | [60] |
| NOTT-112 | 0.05 × 0.05 × 0.05 ($mm^3$) | Single-crystal X-ray | $[Cu_3(C_{54}H_{24}O_{12})$ $(H_2O)_3]$ ·16DMF·$26H_2O$ | [61] |
| MOF-73 | 0.2 × 0.1 × 0.05 ($mm^3$) | Single-crystal X-ray | $Mn_3(BDC)_3$ $(DEF)_2$ | [62] |
| MOF–72 | 0.3 × 0.1 × 0.1 ($mm^3$) | Single-crystal X-ray | $Cd_3$ (1,3–BDC)$_4$•$(Me_2NH_2)_2$ | [62] |
| MOF-70 | 0.22 × 0.20 × 0.18 mm | Single-crystal X-ray | Pb (BDC) $(C_2H_5OH)$·$(C_2H_5OH)$ | [62] |
| TUDMOF-1 | 60–70 nm | PXRD | $Mo_3(BTC)_2$ | [63] |
| MOF-48 | 0.10 × 0.10 × 0.05 ($mm^3$) | Single-crystal X-ray | VO(DMBDC)·$(H_2DMBDC)_{0.4}$ | [64] |
| Ni-MOF-74 | (2.8 nm) | PXRD | $Ni_2$(dhtp) $(H_2O)_2$·$8H_2O$ | [65,66] |
| MIL-53(Al) | (4 μm) | PXRD | Al(OH)$[O_2C–C_6H_4–CO_2]$·$[HO_2C–C_6H_4–CO_2H]_{0.70}$ | [4,33] |
| MIL-101 | 8.87 × 8.87 × 8.87 ($nm^3$) | PXRD | $Cr_3OH(H_2O)_2O(BDC)_3$ | [67] |
| UiO-67 | 75 μm | Single-crystal X-ray | $Zr_6C_{84}H_{48}O_{32}$ | [68,69] |
| POST-1 | 0.15 × 0.5 × 0.5 ($mm^3$) | PXRD + Single-crystal X-ray | $Zn_3$ ($\mu_3$-O) (D-PTT)$_6$ | [70] |
| MIL-125 | 210–660 nm | PXRD | $Ti_{16}O_{72}C_{96}H_{64}$ | [71,72] |
| MIL-100(Fe) | <200 nm | PXRD | $Fe_3O(H_2O)_2F$·$(C_6H_3(CO_2)_3)_2$·$nH_2O$ | [8,73] |
| ZIF-8 | 0.16 × 0.10 × 0.10 $mm^3$ | Single-crystal X-ray | $C_{24}$ $H_{30}$ $N_{12}$ $O_{10}$ $Zn_3$ | [32] |

Materials Institute Lavoisier; UiO = University of Oslo; CPO = Coordination polymer of Oslo; NOTT = Nottingham University; TUDMOF-1 = Technical University of Dresden Metal-Organic Framework, POST = Pohang University of Science and Technology.

**Table 3**
Thermal Stabilities of some selected MOFs.

| MOF | Temperature (K) | Chemical Composition | Type of Solvent and Ligand | Reference |
|---|---|---|---|---|
| MOF-5 | 673–773 | $[Zn_4O(BDC)_3]$ | DMF, $H_2BDC$ | [82,83] |
| MUF-9 | 648–663 | $[Zn_4O$ (*rac*-1$)_3]$ | DMF, rac-$H_2$1 | [84] |
| MOF-2 | 653 | $[Zn_2(BDC)_2(H_2O)_2]$ | DMF, $H_2O$, $H_2BDC$ | [85] |
| IRMOF-10-OH | 623 | $[Zn_4O(BPDC(OH))_3]$ | BPDC-$NH_2$, DEF | [86] |
| MTV-MOF-5-AE | 573 | $[Zn_4O(BDC)_{2.13}(BDC(NO_2))_{0.87}]$ | DEF, DMF, $H_2BDC$-Br | [87] |
| MOF-5 (Zn/Ni) | 723 | $[Zn_{3\cdot64}Ni_{0\cdot36}O(BDC)_3]$ | DMF, $H_2BDC$ | [88] |
| MOF-5 (Zn/Co) | 713 | $[Zn_{3\cdot16}Co_{0\cdot84}O(BDC)_3]$ | DMF, $H_2BDC$ | [89] |
| MOF-801 | 548–873 | $[Zr_6O_8H_4$(fumarate$)_6]$ | DMF, Fumaric acid | [79] |
| Mn-BTT | 473 | Mn3 [(Mn4Cl)3(BTT)8]2·20MeOH | $H_3$BTT. 2HCl, $H_2O$, $CH_3OH$ | [90] |
| Fe-MOF | 553 | $Fe_2(BDP)_3$ | DMF, $H_2BDP$ | [91] |
| $Zn_3(BTP)_2$ | 723 | $Zn_3(BTP)_2$·3DMF·5$CH_3$OH·17$H_2O$ | DMF, Me | [80] |
| IRMOF-3 | 623 | $[Zn_4O(BDC(NH_2))_3]$ | DEF, $H_2BDC$-$NH_2$ | [85] |
| UiO-66 | 753 | $Zr_6O_8H_4(BDC)_6$ | DMF, $H_2BDC$ | [92] |
| UiO-66-F | 678 | $Zr_6O_8H_4$(BDC-F$)_6$ | DMF, $H_2BDC$-F | [93] |
| UiO-66-Cl | 706 | $Zr_6O_8H_4$(BDC-Cl$)_6$ | DMF, $H_2BDC$-Cl | [93] |
| UiO-66-$NH_2$ | 623 | $Zr_6O_8H_4$(BDC-NH2$)_6$ | DMF, $H_2BDC$-$NH_2$ | [94] |
| UiO-66-$NO_2$ | 645 | $Zr_6O_8H_4$ (BDC-NO2$)_6$ | DMF, $H_2BDC$-$NO_2$ | [95] |
| Ti/Zr-MOF | 753 | $(Zr_{6-x}Ti_xO_4(OH)_4(BDC)_6)$ | DMF, BDC | [96] |
| MIL-53(Al) | 803 | Al (OH) ($O_2C$–$C_6H_4$–$CO_2$) | $H_2O$, BDC | [97,98] |
| MIL-96(Al) | 600–800 | $Al_{12}O(OH)_{18}(H_2O)_3(Al_2(OH)_4)$ [btc]$_6$·24$H_2O$. | $H_3$BTC, $H_2O$ | [56] |
| NH2-MIL-53(Al) | 700 | (Al (OH)[$NH_2$-BDC] ·$H_2O$) | $H_2BDC$-$NH_2$, DMF | [99] |

BDC = 1,4-benzene-dicarboxylic acid; DMF = N, *N*-dimethylformamide; MUF = Massey University Framework; IRMOF = Isoreticular MOFs; $H_2BDC$-$NH_2$ = 2-amino-(1,1′-biphenyl)-4,4′-dicarboxylic acid; DEF = *N*,*N*-diethylformamide; MTV = Multivariate metal–organic frameworks; $H_2BDC$-Br = 2,5-bromo-1,3-benzenedicarboxylate; $H_2BDC$-$NO_2$ = 2-nitroterephthalic acid; Fumaric acid = *trans*-1,2-Ethylenedicarboxylic acid; 2-Butenedioic acid; $H_3BTT$·2HCl = 1,3,5-Tris(2H-tetrazol-5-yl)benzene hydrochloride; $CH_3OH$ = Methanol; $H_2BDP$ = 1,4-Di(4′-pyrazolyl)benzene; BTP = 2,6-bis (1,2,3-triazol-4-yl)pyridine; $H_2BDC$-F = 2-Fluoroterephthalic acid; $H_2BDC$-Cl = 2-Chloroterephthalic acid; $H_3BTC$ = 1,3,5-benzenetricarboxylate.

groups are hydrophobic functional groups which impart a high hydrothermal stability to ZIF. However, removal of the methyl groups at temperatures lower than 773 K initiated the decomposition of the imidazole ring, which was destroyed in the temperature range between 873 and 1073 K [81].

Hence, functional groups have a major impact on thermal MOF stability (the thermal stability reduces further when the functional group is a polar functional group). For instance, the thermal breakdown temperature of UiO-66 is 753 K, whereas it is 645, 645 and 623 K for 2OH-UiO-66 [54], $NO_2$-UiO-66 [95] and $NH_2$-UiO-66 [94] respectively). On the other hand, the thermal stabilities of UiO-66 functionalized with halogenic functional groups, such as Cl, F and Br, is only slightly affected [93]. Occasionally (as in MIL-96(Al)), the presence of an uncoordinated organic linker such as BTC inside ultrafine pores can potentially reduce the thermal MOF stability because these molecules might be confined in the MIL-96 (Al) pore network. When they are eliminated from the structure by heating, the whole structure collapses at around 570 K [78].

Generally, TGA experiments determine the mass loss in a sample at a steady heating rate in a specific environment. This mass loss usually occurs in several known steps, starting with dehydration and desolvation at temperatures close to the boiling point of a solvent (<423 K); the mass loss stabilizes when all the solvent is evaporated. During the second step, the solvent and non-reacted precursors are degraded. The degradation of MOFs is represented by the exhaustive third step at the end [100]. For instance, MIL-53(Al, Mn) experienced multi-weight loss steps due to presence of unreacted precursors and solvents (protonated terephthalic acid and metal oxides ($Al_2O_3$ and MnO) as well as the coordinated solvent in the metal centers) inside the pores [98], Fig. 3. Excess precursors are impurities which should be removed from the pores. Such observation is among a special case of synthesized MOFs where unreacted

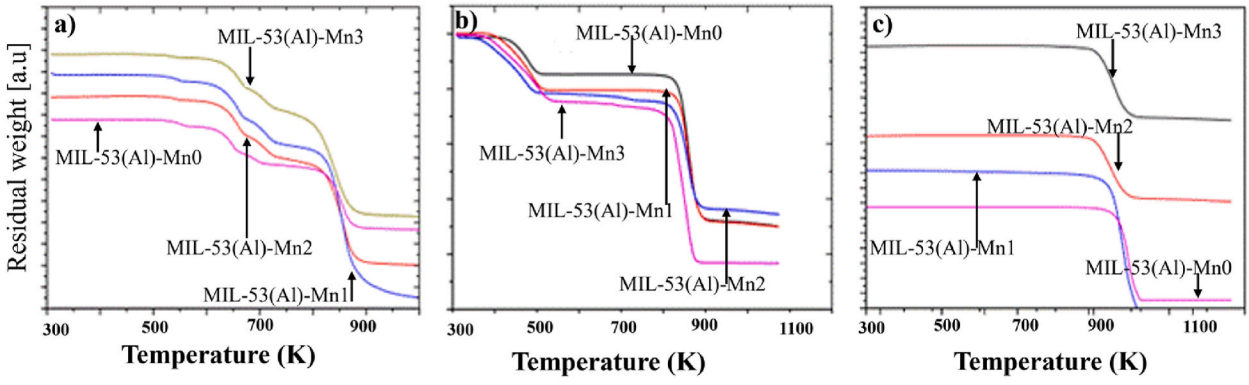


**Fig. 3.** TGA profile of MIL-53 samples a) As synthesized b) Activated solvothermally before heating and c) activated solvothermally after heating.

precursors presented in MOF structure. Therefore, the weight loss steps from 550 to 800 K correspond to the removal of the above-mentioned impurities, while the main weight loss at 800 K represents the starting point of MOF structural breakdown. Furthermore, solvent exchange activation has been confirmed to be the best activation method used for activating MOFs [10], as shown in Table 4. The profiles reveal that these impurities were mainly solvents that weakly interacted with the pores. Consequently, the sample was stable up to approximately 830 K. We conclude that TGA analysis and thermal MOF stability are important factors in the synthesis of MOFs. MOF functionality and structural integrity can be considerably cooperated under different thermal conditions. A limitation in thermal stability makes some MOFs impracticable for certain applications [101] Therefore, the thermal stability of MOFs is a significant factor in determining their performance for the applications of MOFs. Generally, stable MOFs exhibit a high performance over a wide range of applications [102,103].

### 2.3. Pore size analysis and specific surface area

The MOF surface area, pore size, and pore volume are the other key properties of MOF. These quantities are measured via gas adsorption, SAXS, small-angle neutron scattering (SANS), porosimetry, scanning electron microscopy (SEM), or transmission electron microscopy (TEM) [116]. The most widespread method is the gas adsorption method (GAM), which is carried out at the boiling point temperature of the gas and at saturated pressure [117]. Precisely, the pore size is usually indicated as the internal pore width (for slit-like pores) and pore diameter (for cylindrical and spherical pores). Gas physisorption is typically measured through volumetric (manometric) or gravimetric techniques. Gravimetry is more convenient to use for measuring vapor adsorption at room temperature, while volumetry is preferable for measuring nitrogen, krypton, and argon adsorption at cryogenic temperatures (here, 77.4 K and 87.3 K are typical experimental temperatures) [118]. The diffusion of $N_2$ is very slow at low temperature (77 K), and therefore, the analysis requires a long equilibrium time [119], $N_2$ adsorption at 77 K is widely used to measure surface area, pore size, and pore volume if the gas can access small pores (pore >0.7 nm); however, for pores smaller than 0.7 nm, argon (at 87.3 K) is the preferred gas [120]. Nitrogen or argon measurements can routinely measure surface areas as low as 0.5 $m^2\ g^{-1}$, while krypton (at 77 K) is routinely used to analyze even lower surface areas (smaller than <0.05 $m^2\ g^{-1}$) [121]. For pore sizes less than 0.45 nm, carbon dioxide (at 273 K) is used. $CO_2$ (at 298 K) is also used for total pore volume measurements of ultramicropores [120,121]. Note that pores are based on their average size: micropore, mesopore, and macropore. Pore class can be efficiently identified through gas adsorption-desorption isotherms as gas adsorption strongly depends on solid surface characteristics. Thus, the shape of this isotherm refers to the type of the pores and their proportions. The MOF surface areas can be controlled by different benzene chain cross-linkers. Owing to this feature, MOFs with a very high surface area can be synthesized. A high-valence NU-110 E constructed based on a metal-oxo cluster was proved to have an excellent ability to control textural properties [75]. It demonstrated the highest surface area amongst all the MOFs, which was 7140 $m^2\ g^{-1}$ [105].

**Table 4**
Specific surface area of some example MOFs.

| MOF | Specific Surface Area ($m^2\ g^{-1}$) | Organic Linker | Reference |
|---|---|---|---|
| NU-1000 | 2387 | BPDC | [104] |
| NU-110 E | 7140 | $LH_6$-2 | [105] |
| MOF-210 | 6240 | BTE, BPDC | [106] |
| MOF-200 | 4530 | BBC | [106] |
| UiO-68 | 4170 | TPDC | [58] |
| MOF-177 | 3780 | BTB | [107] |
| UiO-67 | 3000 | BPDC | [58] |
| MOF-5-H (DEF/120) | 2766.5 | $H_2$BDC | [108] |
| MOF-5-DMF/$H_2O$–90C | 2136 | $H_2$BDC | [109] |
| MOF-5-L (DMF/130) | 1032.4 | $H_2$BDC | [108] |
| UiO-66 | 1434 | BDC | [92] |
| UiO-66 | 1187 (Langmuir) | BDC | [58] |
| UiO-66-1.9 GPa | 76 | BDC | [110] |
| UiO-66-$NH_2$ | 1220 | $H_2$BDC-$NH_2$ | [94] |
| UiO-66-$(OH)_2$ | 396 | $H_2$BDC-$OH_2$ | [111] |
| UiO-66-$NO_2$ | 771 | $H_2$BDC-$NO_2$ | [111] |
| MIL-100(Fe) | 1604 | BTC | [112] |
| Mg II-MIL-100(Fe) | 1384 | BTC | [112] |
| MIL-53(Al) | 1631.7 | BDC | [98] |
| MIL-53-Mn3 | 1576.38 | BDC | [98] |
| Cu-HKUST-Zn | 1082 | BTC | [113] |
| Cu-HKUST-1-Heating | 1100 | BTC | [114] |
| HKUST-1-Me | 1700 | BTC | [114] |
| MOF-199-Chloroform | 1305 | BTC | [115] |
| MOF-199-Me | 1448 | BTC | [115] |

NU = Northwestern University; $LH_6$ = N,N′-dimethyl-N,N′-ethylene-bis(5-bromo-3-(1H-benzimidazol-2-yl)hydrazineylidene)-2-hydroxybenzylamine); BTE = 4,4′,4″-(1,3,5-benzenetriyltri-2,1-ethynediyl)trisbenzoic acid; BPDC = biphenyl-4,4′-dicarboxylate (BPDC); BBC = 4,4′,44″-[benzene-1,3,5-triyl-tris(benzene-4,1-diyl)]tribenzoate; TPDC = terphenyl dicarboxylate, BTB = (1,3,5-benzenetribenzoate; BPDC = 4,4′ biphenyl-dicarboxylate; $H_2$BDC-$OH_2$ = 2,5 dihydroxybenzenedicarboxylic acid; HKUST = Hong Kong University of Science and Technology.

Similarly, MOF-210, MOF-200 [106], UiO-68 [58], MOF-177 [107], UiO-67 [58] have ultrahigh surface areas; i.e., 6240, 4530, 4170, 3780 and 3000 $m^2 g^{-1}$, respectively. For MOF-200, and MOF-210, the surface area was calculated using Brunauer-Emmett-Teller model (BET), which is less than the surface area calculated by the Langmuir model. The Langmuir isotherm assumes monolayer adsorption in contrast to the multi-layered absorption for the BET model. The synthesis procedure and the solvent used during synthesis can also affect the surface area due to defects produced in the MOF structures. A prime example for this phenomenon is MOF-5, which was synthesized by using DEF as a solvent (resulting in a surface area of 2766.5 $m^2 g^{-1}$ [108]). Changing the solvent to DMF resulted in the synthesis of MOF-5 having a low surface area (1032.4 $m^2 g^{-1}$) [108]. However, using $H_2O$ with DMF as a co-solvent to synthesize MOF-5 increased the surface area (again to 2136 $m^2 g^{-1}$) [109], Table 3.

Sample preparation for pore size analysis and degassing conditions (temperature and evacuation rate) is an extremely important factor to ensure MOF integrity during degassing process [105]. The degassing temperature should be lower than 75 % of the MOF decomposition temperature. Also, the surface area is significantly affected by the activation process. To access the full surface area, solvent-filled materials are initially evacuated through a selective activation process without pore collapse [122]. Activation by heating [10], results in a low MOF surface area because the structure undergoes a partial breakdown and/or the pores are not completely cleaned from the solvent and unreacted precursors. Table 3 demonstrates selective MOFs, such as HKUST-1, MOF-199, and UiO-66, which are activated through heating and solvent exchange methods. A typical example is the $N_2$ adsorption-desorption isothermal behavior of HKUST-1 at 77 K (Fig. 4) after activation by methanol exchange method. It should be noted that a sharp decrease in $N_2$ adsorption is observed at low relative pressure, indicating a significant increase in the micropore content, and consequently, an enlarged surface area (from 1100 $m^2 g^{-1}$ after activation by heating to 1700 $m^2 g^{-1}$ after methanol exchange activation), while the mesopore size decreased from 4.5 nm to 2 nm (Fig. 4b [114]). This indicates that the methanol molecules can efficiently eliminate impurities from HKUST-1 and open ultra-micropores. The high polarity of methanol makes it one of the most suitable solvents (compared to $CHCl_3$, $CH_2Cl_2$, acetone, DMF, ethanol, and water) to maximize the surface area of HKUST-1 [123,124].

It is noteworthy that the high mechanical compression of the MOF may cause a diminishment of the free pore volume, and a huge decrease in the surface area and porosity due to breakage of chemical bonds. This trend has been demonstrated for UiO-66, where the surface area significantly dropped after the application of mechanical pressures of around 1.9 GPa [110].

Furthermore, the surface area can also be reduced by using a high concentration of a second metal in bimetallic organic-frameworks; some examples of this behavior are Mg-MIL-100(Fe) [112], MIL-53(Al)–Mn3 [98] and Cu-HKUST-Zn [113], Table 4.

Amongst other MOF materials represented by NU-1000, Zr-MOF exhibits excellent textural properties, including a high surface and large pore size, which makes it a promising material for various applications. These include gas storage, drug delivery, water remediation, energy storage, multi-phase catalysis, and electrocatalysis [104].

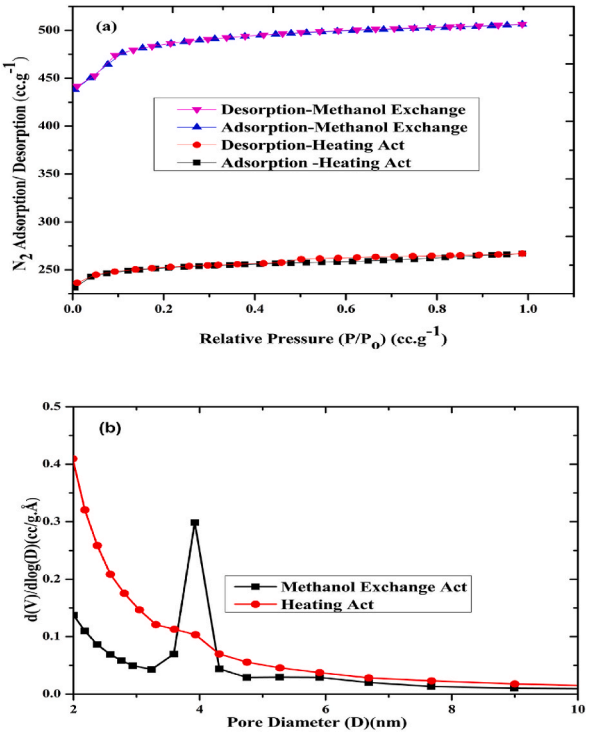


**Fig. 4. A)** $N_2$ Adsorption/Desorption isotherms and b) Mesoporous pore size distribution of HKUST-1 with different activation method.

### 2.4. Surface functional groups

Functional groups are molecular moieties of a specific stoichiometry, which typically undergo similar chemical reactions that occur in most molecules containing these moieties. In organic chemistry, a functional group is used to characterize and classify molecules and estimate their reactions. Each functional group can exhibit similar physical and chemical reactions [125]. Surface functional groups play a prominent role in the performance of porous carbon and MOF [126,127] particularly in adsorption processes. Fourier Transform Infrared (FTIR) spectroscopy is typically used to identify such surface functional groups, and FTIR measures the change in dipole moment versus the chemical bond length. FTIR is thus used initially during MOF synthesis to identify impurities and residual reactants on external surfaces and pores in the interior [128]; Non-reacted organic linker and coordinated solvent in the MOF structures can easily be identified through FTIR. For instance, when terephthalic acids or their derivatives are used for MOF synthesis, the carboxylic group (-$CO_2$) in cross-linked terephthalic acid is shown as an FTIR peak band at 1400–1767 $cm^{-1}$, while non-reacted terephthalic acid exhibits a band at 1650–1767 $cm^{-1}$ [4]. The progress of the reaction can also be observed via FTIR when IR-peaks of the organic linkers and coordinated solvents are diminished in the spectrum of the activated sample [94,129]. As shown in Fig. 5, $CO_2H$ groups appear at 1659 $cm^{-1}$ in 2OH-UiO-66, $NO_2$-UiO-66, and $NH_2$-UiO-66 before activation but disappear after activation. Specifically, a peak of hydroxyl group at 3300 $cm^{-1}$ and an absorption band of OH in-plane deformation at 1460 $cm^{-1}$ were observed [94,111]. In addition, an asymmetric ($\nu$(NO) *asym*) peak was observed at 1544 $cm^{-1}$ (which identifies $NO_2$ groups). *C*–N stretching of an aromatic amine was observed at 1356 $cm^{-1}$ [95], and a primary amine was identified by two peaks at 3376 and 3457 $cm^{-1}$ [94], shown in Fig. 5. Furthermore, the existence of crystalline MOF was confirmed by the observation of four peaks at 1300–1630 $cm^{-1}$ (metal oxide-terephthalate bond), the presence of –$CO_2$ asymmetrical stretching at 1497 and 1600 $cm^{-1}$, and –$CO_2$ symmetrical stretching at 1391 and 1408 $cm^{-1}$ [130,131]. Table 5 displays the infrared data for –$CO_2$ functional groups in various MOFs.

Functional groups inside the pores of MOFs play a major role in their chemical modifications. Specifically, post-synthesis modification of MOFs is facilely achieved with the presence of functional groups on the organic linkers, and it is significantly affected by the nature, size, and number of these functional groups [136]. Functional groups can also be tuned on the surface of MOFs via different ways. One of the methods is through direct synthesis procedure [94]. The other ways are post-synthesis modification [10] and chemical etching modification [136]. The pore parameters and functional groups cooperatively operate in the applications of MOFs. Therefore, changing the functional group leads to a change in the pore structure. Based on the type of the functional group, MOFs can be used in various applications, such as gas storage, catalysis, sensing, separation, and drug delivery [137].

## 3. Outlook and future directions

This paper conducts a systematic review of the essential physicochemical properties of Metal-Organic Frameworks (MOFs), with an emphasis on facilitating the research journey for novice researchers. The review covers key MOF characterization techniques, including X-ray Diffraction (XRD), Thermogravimetric Analysis (TGA), assessments of textural properties, and Fourier-transform infrared (FTIR) spectroscopy.

XRD enables the identification of MOF structures and integrity, while TGA provides insights into MOF thermal degradation profiles and decomposition temperatures, highlighting the significance of thermal stability in selecting appropriate preparation conditions for MOFs. Furthermore, it is noted that the factors influencing the MOF surface area include the synthesis procedure (type of solvents, cross-linkers, second metal, and temperature), the activation method, and mechanical pressure.

FTIR spectra, employed to identify active functional MOF groups, such as –$CO_2$, –NO, –OH, –$NH_2$, or –CN, are crucial to understanding MOF stability. The robustness of the FTIR technique is exemplified through its applicability to powder samples, thin films, and fully fabricated devices, rendering it a standard, effective method to verify functional groups in MOFs.

With regard to studies that are primarily focused on synthesis, the researchers who work on MOF should pay greater attention to simplified and authentic in situ FTIR measurement processes or techniques. XRD measurements for thin films can be challenging on crystalline or amorphous substrates due to strong signals from the substrates [138]. Therefore, alternative techniques such as High-Resolution Transmission Electron Microscopy (HR-TEM) may verify the crystalline structure, albeit with less effectiveness for novel MOFs as compared to MOF powders that have been investigated extensively [139].

MOF thin films, produced through direct synthesis routes or post-synthetically modified methods, require sophisticated techniques such as Atomic Force Microscopy for investigation of their porosity. For MOF-derived materials (both powders and thin films) in electrochemical applications like fuel cells, batteries, water splitting, and supercapacitors, more attention should be given to the electrochemically active surface area as opposed to the geometric or specific surface area [140].

The doping of heteroatoms and incorporation of external moieties in existing MOF structures can be elucidated by HR-TEM and Energy Dispersive Spectroscopy (EDS). The trademark properties of MOFs, such as porosity and geometric surface area, are usually reported through gas adsorption isotherms using nitrogen as an adsorbate due to its inert nature and readily available property data. However, discrepancies can arise in reporting surface area, pore size, pore volume, and pore size distribution based on $N_2$ isotherms [141]. A comparison of the intrinsic density of perfectly structured MOFs and that of the actual bulk synthesized ones can assist in evaluating synthesis accuracy and the role of activation for powder samples. These characteristics are paramount in the selection of MOFs for specific applications, especially when developing novel MOFs.

In summary, this review critically examines MOF characterization techniques, providing a comprehensive and accessible overview for new researchers in this area. Consequently, it will contribute to the improvement of MOF development techniques and their characterization for targeted applications. For future work, a review of the characterization of MOFs under high pressures and high temperatures is recommended.

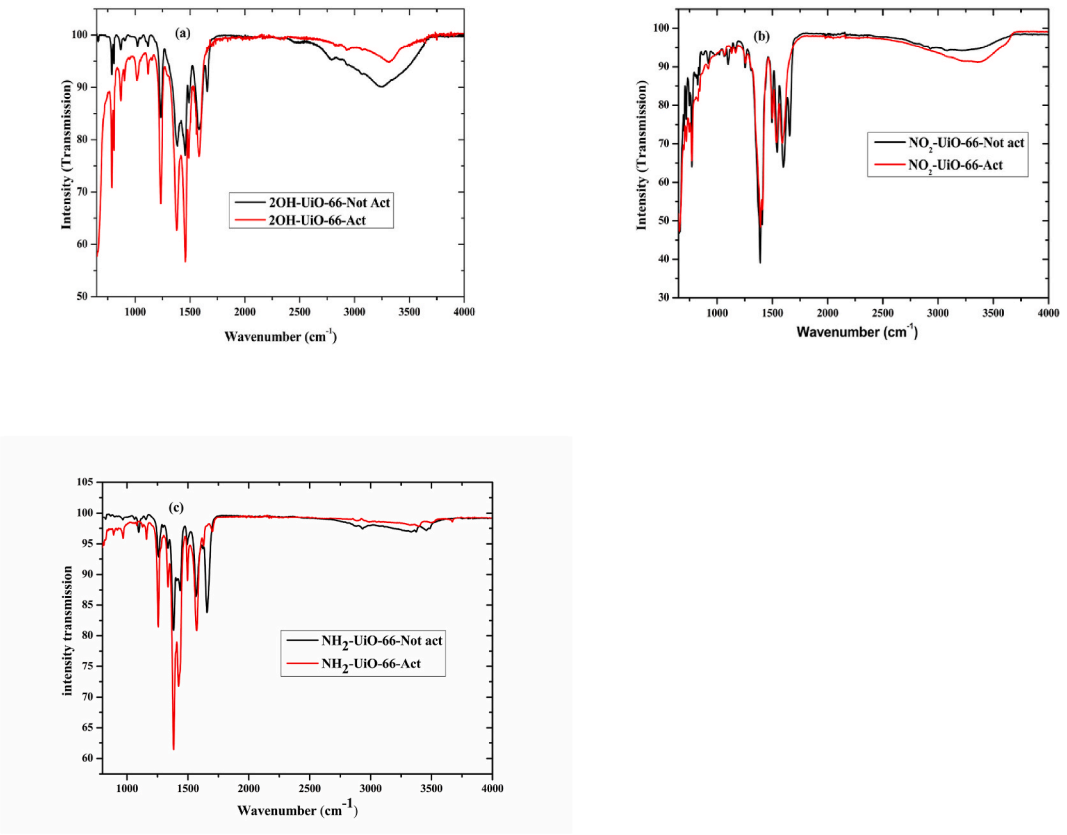


**Fig. 5.** FTIR spectra of UiO-66 MOFs with various surface functional groups a) OH-UiO-66, b) $NO_2$-UiO-66 and c) $NH_2$-UiO-66.

**Table 5**
FTIR absorption frequencies of some selected MOFs.

| MOFs | Organic Linker | FTIR Absorption Frequency ($cm^{-1}$) | | Reference |
|---|---|---|---|---|
| | | Not Coordinated<br>-$CO_2H$ | Coordinated<br>-$CO_2$ Asymmetrical Stretching<br>-$CO_2$ Symmetrical Stretching | |
| UiO-66-Zr | BDC | 1670 | 1584; 1393 | [92,129] |
| NH2-UiO-66-Zr | $NH_2$-BDC | 1656 | 1497,1564; 1385,1424 | [94] |
| MIL-53-Al | BDC | 1730–1650 | 1574,1505; 1443,1397 | [4] |
| MIL-96-Al | BTC | 1654 | 1597; 1457,1396 | [4] |
| $NH_2$-MIL-53 | $NH_2$-BDC | 1688 | 1565, 1494; 1440, 1389 | [4] |
| MOF-5-Zn | BDC | 1654 | 1608,1540; 1410,1340 | [132] |
| HKUST-1 | BTC | 1700 | 1450,1649; 1373,1548 | [114,133] |
| MIL-100 (Fe) | BTC | 1750 | 1690: Nil | [8] |
| NH2-MIL-101(Fe) | $NH_2$-BDC | 1659 | 1583; 1436 | [131] |
| NO2-UiO-66 (Zr) | BDC-$NO_2$ | 1650 | 1590,1495; 1409,1389 | [111] |
| 2OH-UiO-66 (Zr) | BDC-$OH_2$ | 1659 | 1500; 1380 | [54] |
| MIL-47($V^{III}$) | BDC | 1695–1708 | 1542,1566; 1393, 1420 | [134] |
| MIL-101(Cr) | BDC | 1700 | Nil; 1404 | [135] |

## 4. Data availability statement

No data was used for the research described in this article.

## Funding

This research received no external funding.

## CRediT authorship contribution statement

**Hussein Rasool Abid:** Writing – original draft, Visualization, Software, Investigation, Conceptualization. **Muhammad Rizwan Azhar:** Writing – review & editing, Writing – original draft, Software, Conceptualization. **Stefan Iglauer:** Writing – review & editing, Supervision, Resources. **Zana Hassan Rada:** Writing – review & editing, Software. **Ahmed Al-Yaseri:** Writing – review & editing. **Alireza Keshavarz:** Supervision, Resources.

## Declaration of competing interest

The authors declare that they have no known competing financial interests or personal relationships that could have appeared to influence the work reported in this paper.

## References


[1] N. Hanikel, M.S. Prévot, F. Fathieh, E.A. Kapustin, H. Lyu, H. Wang, N.J. Diercks, T.G. Glover, O.M. Yaghi, Rapid cycling and exceptional yield in a metal-organic framework water harvester, ACS Cent. Sci. 5 (10) (2019) 1699–1706.

[2] Y. Kamakura, D. Tanaka, Metal–organic frameworks and coordination polymers composed of sulfur-based nodes, Chem. Lett. 50 (3) (2021) 523–533.

[3] V.F. Yusuf, N.I. Malek, S.K. Kailasa, 15 - fluorescent metal-organic frameworks for analytical applications, in: J.R. Koduru, R.R. Karri, N.M. Mubarak (Eds.), Hybrid Nanomaterials for Sustainable Applications, Elsevier, 2023, pp. 339–374.

[4] H.R. Abid, Z.H. Rada, J. Shang, S. Wang, Synthesis, characterization, and CO2 adsorption of three metal-organic frameworks (MOFs): MIL-53, MIL-96, and amino-MIL-53, Polyhedron 120 (2016) 103–111.

[5] V. Pascanu, G. González Miera, A.K. Inge, B. Martín-Matute, Metal–organic frameworks as catalysts for organic synthesis: a critical perspective, J. Am. Chem. Soc. 141 (18) (2019) 7223–7234.

[6] H.-Y. Li, S.-N. Zhao, S.-Q. Zang, J. Li, Functional metal–organic frameworks as effective sensors of gases and volatile compounds, Chem. Soc. Rev. 49 (17) (2020) 6364–6401.

[7] M.R. Azhar, G. Hussain, M.O. Tade, D.S. Silvester, S. Wang, Electrodeposited metal organic framework toward excellent hydrogen sensing in an ionic liquid, ACS Appl. Nano Mater. 3 (5) (2020) 4376–4385.

[8] M. Al Haydar, H.R. Abid, B. Sunderland, S. Wang, Metal organic frameworks as a drug delivery system for flurbiprofen, Drug Des. Dev. Ther. 11 (2017) 2685–2695.

[9] Y.-R. Lee, J. Kim, W.-S. Ahn, Synthesis of metal-organic frameworks: a mini review, Kor. J. Chem. Eng. 30 (9) (2013) 1667–1680.

[10] N. Al Amery, H.R. Abid, S. Al-Saadi, S. Wang, S. Liu, Facile directions for synthesis, modification and activation of MOFs, Mater. Today Chem. 17 (2020), 100343.

[11] M. Dehghankar, R. Hmtshirazi, T. Mohammadi, M.A. Tofighy, Synthesis and modification methods of metal-organic frameworks and their application in modification of polymeric ultrafiltration membranes: a review, J. Environ. Chem. Eng. 11 (3) (2023), 109954.

[12] Y. Rao, Z. Kou, X. Zhang, P. Lu, Metal organic framework glasses: a new platform for electrocatalysis? Chem. Rec. (2023), e202200251.

[13] X.T. Liu, B.B. Qian, D.S. Zhang, M.H. Yu, Z. Chang, X.H. Bu, Recent progress in host–guest metal–organic frameworks: construction and emergent properties, Coord. Chem. Rev. (2023) 476.

[14] W. Qu, C. Chen, Z. Tang, H. Wen, L. Hu, D. Xia, S. Tian, H. Zhao, C. He, D. Shu, Progress in metal-organic-framework-based single-atom catalysts for environmental remediation, Coord. Chem. Rev. (2023) 474.

[15] X. Zhao, S. He, B. Li, B. Liu, Y. Shi, W. Cong, F. Gao, J. Li, F. Wang, K. Liu, C. Sheng, J. Su, H.-G. Hu, DUCNP@Mn–MOF/FOE as a highly selective and bioavailable drug delivery system for synergistic combination cancer therapy, Nano Lett. 23 (3) (2023) 863–871.

[16] M.R. Saeb, N. Rabiee, M. Mozafari, F. Verpoort, L.G. Voskressensky, R. Luque, Metal-organic frameworks (MOFs) for cancer therapy, Materials 14 (23) (2021).

[17] S.I. Abdelsalam, A. Magesh, P. Tamizharasi, A. Zaher, Versatile response of a Sutterby nanofluid under activation energy: hyperthermia therapy, Int. J. Numer. Methods Heat Fluid Flow (2023), https://doi.org/10.1108/HFF-04-2023-0173. Vol. ahead-of-print No. ahead-of-print.

[18] N.H. Abdelhamid, Zeolitic imidazolate frameworks (ZIF-8) for biomedical applications: a review, Curr. Med. Chem. 28 (34) (2021) 7023–7075.

[19] T. Jia, Y. Gu, F. Li, Progress and potential of metal-organic frameworks (MOFs) for gas storage and separation: a review, J. Environ. Chem. Eng. 10 (5) (2022), 108300.

[20] Z.R. Herm, J.A. Swisher, B. Smit, R. Krishna, J.R. Long, Metal– organic frameworks as adsorbents for hydrogen purification and precombustion carbon dioxide capture, J. Am. Chem. Soc. 133 (15) (2011) 5664–5667.

[21] A. Zuliani, N. Khiar, C. Carrillo-Carrión, Recent progress of metal–organic frameworks as sensors in (bio)analytical fields: towards real-world applications, Anal. Bioanal. Chem. 415 (11) (2023) 2005–2023.

[22] H. Sohrabi, S. Ghasemzadeh, Z. Ghoreishi, M.R. Majidi, Y. Yoon, N. Dizge, A. Khataee, Metal-organic frameworks (MOF)-based sensors for detection of toxic gases: a review of current status and future prospects, Mater. Chem. Phys. 299 (2023), 127512.

[23] R.E. Malekshah, M. Moharramnejad, S. Gharanli, M. Shahi, A. Ehsani, J. Haribabu, H. Ouachtak, B. Mirtamizdoust, K. Kamwilaisak, M. Sillanpää, H. Erfani, MOFs as versatile catalysts: synthesis strategies and applications in value-added compound production, ACS Omega 8 (35) (2023) 31600–31619.

[24] H. Konnerth, B.M. Matsagar, S.S. Chen, M.H.G. Prechtl, F.-K. Shieh, K.C.W. Wu, Metal-organic framework (MOF)-derived catalysts for fine chemical production, Coord. Chem. Rev. 416 (2020), 213319.

[25] 3. Crystal structure determination, in: K. Lark-Horovitz, V.A. Johnson (Eds.), Methods in Experimental Physics, Academic Press, 1959, pp. 187–282.

[26] A.D. Katsenis, A. Puskaric, V. Strukil, C. Mottillo, P.A. Julien, K. Uzarevic, M.H. Pham, T.O. Do, S.A. Kimber, P. Lazic, O. Magdysyuk, R.E. Dinnebier, I. Halasz, T. Friscic, In situ X-ray diffraction monitoring of a mechanochemical reaction reveals a unique topology metal-organic framework, Nat. Commun. 6 (2015) 6662.

[27] M. Kalaj, K.C. Bentz, S. Ayala Jr., J.M. Palomba, K.S. Barcus, Y. Katayama, S.M. Cohen, MOF-polymer hybrid materials: from simple composites to tailored architectures, Chem Rev 120 (16) (2020) 8267–8302.

[28] G.G. Zhang, D. Zhou, Crystalline and amorphous solids, in: Developing Solid Oral Dosage Forms, Elsevier, 2017, pp. 23–57.

[29] R.L. Harlow, Single-crystal X-ray diffraction, in: R.E. Whan (Ed.), Materials Characterization, ASM International, 1986, p. 0.

[30] M.M. Font Bardia, X. Alcobé i Ollé, X-ray single crystal and powder diffraction: possibilities and applications. Capítol del llibre: Handbook of instrumental techniques for materials, chemical and biosciences research, Centres Científics i Tecnològics, vol. 9, Universitat de Barcelona, Barcelona, 2012, p. 14, 2012. Part I. Materials technologies (MT), MT.

[31] T.W. Ni, M.A. Tofanelli, C.J. Ackerson, Chapter 5 - structure determination by single crystal X-ray crystallography, in: T. Tsukuda, H. Häkkinen (Eds.), Frontiers of Nanoscience, Elsevier, 2015, pp. 103–125.

[32] K.S. Park, Z. Ni, A.P. Côté, J.Y. Choi, R. Huang, F.J. Uribe-Romo, H.K. Chae, M. O'Keeffe, O.M. Yaghi, Exceptional chemical and thermal stability of zeolitic imidazolate frameworks, Proc. Natl. Acad. Sci. USA 103 (27) (2006) 10186–10191.

[33] T. Loiseau, C. Serre, C. Huguenard, G. Fink, F. Taulelle, M. Henry, T. Bataille, G. Férey, A rationale for the large breathing of the porous aluminum terephthalate (MIL-53) upon hydration, Chem. Eur J. 10 (6) (2004) 1373–1382.

[34] N. Ahadi, S. Askari, A. Fouladitajar, I. Akbari, Facile synthesis of hierarchically structured MIL-53(Al) with superior properties using an environmentally-friendly ultrasonic method for separating lead ions from aqueous solutions, Sci. Rep. 12 (1) (2022) 2649.
[35] M.M. Hulagabali, A.V. Sonawane, G.R. Vesmawala, Synthesis, characterization, and application of ZIF-67 metal-organic framework to enhance the microstructure and compressive strength of cement composite, J. Mater. Civ. Eng. 35 (5) (2023), 04023090.
[36] N. Iwashita, Chapter 2 - X-ray powder diffraction, in: M. Inagaki, F. Kang (Eds.), Materials Science and Engineering of Carbon, Butterworth-Heinemann, 2016, pp. 7–25.
[37] G.A. Jeffrey, M. Sax, X-ray diffraction, crystal structure analysis, and the high-speed computer, Anal. Chem. 34 (5) (1962) 339R–343r.
[38] C. Giannini, M. Ladisa, D. Altamura, D. Siliqi, T. Sibillano, L. De Caro, X-Ray diffraction: a powerful technique for the multiple-length-scale structural analysis of nanomaterials, Crystals 6 (8) (2016) 87.
[39] H. Cheng, C. Lu, J. Liu, Y. Yan, X. Han, H. Jin, Y. Wang, Y. Liu, C. Wu, Synchrotron radiation X-ray powder diffraction techniques applied in hydrogen storage materials - a review, Prog. Nat. Sci.: Mater. Int. 27 (1) (2017) 66–73.
[40] J.t. Nijenhuis, M. Gateshki, M.J. Fransen, Possibilities and limitations of X-ray diffraction using high-energy X-rays on a laboratory system, in: Eleventh European Powder Diffraction Conference, Oldenbourg Wissenschaftsverlag, München, 2009, pp. 163–170.
[41] A. Schaate, P. Roy, A. Godt, J. Lippke, F. Waltz, M. Wiebcke, P. Behrens, Modulated synthesis of Zr-based metal–organic frameworks: from nano to single crystals, Chem. Eur J. 17 (24) (2011) 6643–6651.
[42] K. Barmak, K. Coffey, Metallic Films for Electronic, Optical and Magnetic Applications: Structure, Processing and Properties, Woodhead Publishing, 2014.
[43] N. Tamura, P.U. Gilbert, X-ray microdiffraction of biominerals, in: Methods in Enzymology, Elsevier, 2013, pp. 501–531.
[44] S. Da Vela, D.I. Svergun, Methods, development and applications of small-angle X-ray scattering to characterize biological macromolecules in solution, Curr Res Struct Biol 2 (2020) 164–170.
[45] T. Li, A.J. Senesi, B. Lee, Small angle X-ray scattering for nanoparticle research, Chem. Rev. 116 (18) (2016) 11128–11180.
[46] W. Bras, I.P. Dolbnya, D. Detollenaere, R. van Tol, M. Malfois, G.N. Greaves, A.J. Ryan, E. Heeley, Recent experiments on a small-angle/wide-angle X-ray scattering beam line at the ESRF, J. Appl. Crystallogr. 36 (3) (2003) 791–794.
[47] C. Santos, E. Senokos, J.C. Fernández-Toribio, Á. Ridruejo, R. Marcilla, J.J. Vilatela, Pore structure and electrochemical properties of CNT-based electrodes studied by in situ small/wide angle X-ray scattering, J. Mater. Chem. A 7 (10) (2019) 5305–5314.
[48] J. Bolze, M. Ballauff, J. Kijlstra, D. Rudhardt, Application of small-angle X-ray scattering as a tool for the structural analysis of industrial polymer dispersions, Macromol. Mater. Eng. 288 (6) (2003) 495–502.
[49] J. Polte, R. Erler, A.F. Thunemann, S. Sokolov, T.T. Ahner, K. Rademann, F. Emmerling, R. Kraehnert, Nucleation and growth of gold nanoparticles studied via in situ small angle X-ray scattering at millisecond time resolution, ACS Nano 4 (2) (2010) 1076–1082.
[50] A. Braun, F.E. Huggins, S. Seifert, J. Ilavsky, N. Shah, K.E. Kelly, A. Sarofim, G.P. Huffman, Size-range analysis of diesel soot with ultra-small angle X-ray scattering, Combust. Flame 137 (1) (2004) 63–72.
[51] A. Agbabiaka, M. Wiltfong, C. Park, Small angle X-ray scattering technique for the particle size distribution of nonporous nanoparticles, Journal of Nanoparticles (2013) 2013.
[52] I.W. Hamley, Small-angle Scattering: Theory, Instrumentation, Data, and Applications, John Wiley & Sons, 2021.
[53] M. Kandiah, M.H. Nilsen, S. Usseglio, S. Jakobsen, U. Olsbye, M. Tilset, C. Larabi, E.A. Quadrelli, F. Bonino, K.P. Lillerud, Synthesis and stability of tagged UiO-66 Zr-MOFs, Chem. Mater. 22 (24) (2010) 6632–6640.
[54] S. Zaboon, H.R. Abid, Z. Yao, R. Gubner, S. Wang, A. Barifcani, Removal of monoethylene glycol from wastewater by using Zr-metal organic frameworks, J. Colloid Interface Sci. 523 (2018) 75–85.
[55] H.R. Abid, Z.H. Rada, X. Duan, H. Sun, S. Wang, *Enhanced* $CO_2$ adsorption and selectivity of $CO_2/N_2$ on Amino-MIL-53 (Al) synthesized by polar co-solvents, Energy & fuels 32 (4) (2017) 4502–4510.
[56] T. Loiseau, L. Lecroq, C. Volkringer, J. Marrot, G. Férey, M. Haouas, F. Taulelle, S. Bourrelly, P.L. Llewellyn, M. Latroche, MIL-96, a porous aluminum trimesate 3D structure constructed from a hexagonal network of 18-membered rings and μ3-oxo-centered trinuclear units, J. Am. Chem. Soc. 128 (31) (2006) 10223–10230.
[57] H. Li, M. Eddaoudi, M. O'Keeffe, O.M. Yaghi, Design and synthesis of an exceptionally stable and highly porous metal-organic framework, Nature 402 (6759) (1999) 276–279.
[58] J.H. Cavka, S. Jakobsen, U. Olsbye, N. Guillou, C. Lamberti, S. Bordiga, K.P. Lillerud, A new zirconium inorganic building brick forming metal organic frameworks with exceptional stability, J. Am. Chem. Soc. 130 (42) (2008) 13850–13851.
[59] P.T.K. Nguyen, H.T.D. Nguyen, H.N. Nguyen, C.A. Trickett, Q.T. Ton, E. Gutiérrez-Puebla, M.A. Monge, K.E. Cordova, F. Gándara, New metal–organic frameworks for chemical fixation of CO2, ACS Appl. Mater. Interfaces 10 (1) (2018) 733–744.
[60] P.D.C. Dietzel, Y. Morita, R. Blom, H. Fjellvåg, An in situ high-temperature single-crystal investigation of a dehydrated metal–organic framework compound and field-induced magnetization of one-dimensional metal–oxygen chains, Angew. Chem. Int. Ed. 44 (39) (2005) 6354–6358.
[61] Y. Yan, I. Telepeni, S. Yang, X. Lin, W. Kockelmann, A. Dailly, A.J. Blake, W. Lewis, G.S. Walker, D.R. Allan, S.A. Barnett, N.R. Champness, M. Schröder, Metal−Organic polyhedral frameworks: high H2 adsorption capacities and neutron powder diffraction studies, J. Am. Chem. Soc. 132 (12) (2010) 4092–4094.
[62] N.L. Rosi, J. Kim, M. Eddaoudi, B. Chen, M. O'Keeffe, O.M. Yaghi, Rod packings and Metal−Organic frameworks constructed from rod-shaped secondary building units, J. Am. Chem. Soc. 127 (5) (2005) 1504–1518.
[63] M. Kramer, U. Schwarz, S. Kaskel, Synthesis and properties of the metal-organic framework Mo3(BTC)2 (TUDMOF-1), J. Mater. Chem. 16 (23) (2006) 2245–2248.
[64] A. Phan, A.U. Czaja, F. Gándara, C.B. Knobler, O.M. Yaghi, Metal–organic frameworks of vanadium as catalysts for conversion of methane to acetic acid, Inorg. Chem. 50 (16) (2011) 7388–7390.
[65] Leaf-nosed Bat, in Encyclopædia Britannica, Encyclopædia Britannica Online, 2009.
[66] M. Díaz-García, Á. Mayoral, I. Díaz, M. Sánchez-Sánchez, Nanoscaled M-MOF-74 materials prepared at room temperature, Cryst. Growth Des. 14 (5) (2014) 2479–2487.
[67] G. Ferey, C. Mellot-Draznieks, C. Serre, F. Millange, J. Dutour, S. Surble, I. Margiolaki, A chromium terephthalate-based solid with unusually large pore volumes and surface area, Science 309 (5743) (2005) 2040–2042.
[68] S. Chavan, J.G. Vitillo, D. Gianolio, O. Zavorotynska, B. Civalleri, S. Jakobsen, M.H. Nilsen, L. Valenzano, C. Lamberti, K.P. Lillerud, S. Bordiga, H2storage in isostructural UiO-67 and UiO-66 MOFs, Phys. Chem. Chem. Phys. 14 (5) (2012) 1614–1626.
[69] S. Øien, D. Wragg, H. Reinsch, S. Svelle, S. Bordiga, C. Lamberti, K.P. Lillerud, Detailed structure analysis of atomic positions and defects in zirconium metal–organic frameworks, Cryst. Growth Des. 14 (11) (2014) 5370–5372.
[70] J.S. Seo, D. Whang, H. Lee, S.I. Jun, J. Oh, Y.J. Jeon, K. Kim, A homochiral metal–organic porous material for enantioselective separation and catalysis, Nature 404 (6781) (2000) 982–986.
[71] M. Dan-Hardi, C. Serre, T. Frot, L. Rozes, G. Maurin, C. Sanchez, G. Férey, A new photoactive crystalline highly porous titanium(IV) dicarboxylate, J. Am. Chem. Soc. 131 (31) (2009) 10857–10859.
[72] S.M.F. Vilela, P. Salcedo-Abraira, I. Colinet, F. Salles, M.C. de Koning, M.J.A. Joosen, C. Serre, P. Horcajada, Nanometric MIL-125-nh₂ metal-organic framework as a potential nerve agent antidote carrier, Nanomaterials 7 (10) (2017) 321.
[73] P. Horcajada, S. Surblé, C. Serre, D.-Y. Hong, Y.-K. Seo, J.-S. Chang, J.-M. Grenèche, I. Margiolaki, G. Férey, Synthesis and catalytic properties of MIL-100(Fe), an iron(iii) carboxylate with large pores, Chem. Commun. (27) (2007) 2820–2822.
[74] M.J. Turk, A.S. Ansari, W.B. Alston, G.S. Gahn, A.A. Frimer, D.A. Scheiman, Evaluation of the thermal oxidative stability of polyimides via TGA techniques, J. Polym. Sci. Polym. Chem. 37 (21) (1999) 3943–3956.
[75] C. Wang, J. Yan, S. Chen, Y. Liu, High-valence metal-organic framework materials constructed from metal-oxo clusters: opportunities and challenges, ChemPlusChem 88 (3) (2023), e202200462.

[76] A.J. Howarth, Y. Liu, P. Li, Z. Li, T.C. Wang, J.T. Hupp, O.K. Farha, Chemical, thermal and mechanical stabilities of metal–organic frameworks, Nat. Rev. Mater. 1 (3) (2016), 15018.
[77] M. Bosch, M. Zhang, H.-C. Zhou, Increasing the stability of metal-organic frameworks, Advances in Chemistry 2014 (2014) 8.
[78] I.J. Kang, N.A. Khan, E. Haque, S.H. Jhung, Chemical and thermal stability of isotypic metal–organic frameworks: effect of metal ions, Chem. Eur J. 17 (23) (2011) 6437–6442.
[79] G. Wißmann, A. Schaate, S. Lilienthal, I. Bremer, A.M. Schneider, P. Behrens, Modulated synthesis of Zr-fumarate MOF, Microporous Mesoporous Mater. 152 (2012) 64–70.
[80] V. Colombo, S. Galli, H.J. Choi, G.D. Han, A. Maspero, G. Palmisano, N. Masciocchi, J.R. Long, High thermal and chemical stability in pyrazolate-bridged metal–organic frameworks with exposed metal sites, Chem. Sci. 2 (7) (2011) 1311–1319.
[81] S. Gadipelli, Z.X. Guo, *Tuning of ZIF-derived Carbon with high activity, nitrogen functionality, and yield – a Case for superior $CO_2$* capture, ChemSusChem 8 (12) (2015) 2123–2132.
[82] S. Gadipelli, Z. Guo, Postsynthesis Annealing of MOF-5 remarkably Enhances the framework structural Stability and CO2 uptake, Chem. Mater. 26 (22) (2014) 6333–6338.
[83] W. Zhen, B. Li, G. Lu, J. Ma, Enhancing catalytic activity and stability for $CO_2$ methanation on Ni@MOF-5 via control of active species dispersion, Chem. Commun. 51 (9) (2015) 1728–1731.
[84] A. Ferguson, L. Liu, S.J. Tapperwijn, D. Perl, F.-X. Coudert, S. Van Cleuvenbergen, T. Verbiest, M.A. van der Veen, S.G. Telfer, Controlled partial interpenetration in metal–organic frameworks, Nat. Chem. 8 (3) (2016) 250–257.
[85] A.R. Millward, O.M. Yaghi, Metal−Organic frameworks with exceptionally high capacity for storage of carbon dioxide at room temperature, J. Am. Chem. Soc. 127 (51) (2005) 17998–17999.
[86] R.K. Deshpande, G.I.N. Waterhouse, G.B. Jameson, S.G. Telfer, Photolabile protecting groups in metal–organic frameworks: preventing interpenetration and masking functional groups, Chem. Commun. 48 (10) (2012) 1574–1576.
[87] H. Deng, C.J. Doonan, H. Furukawa, R.B. Ferreira, J. Towne, C.B. Knobler, B. Wang, O.M. Yaghi, Multiple functional groups of varying ratios in metal-organic frameworks, Science 327 (5967) (2010) 846–850.
[88] C.K. Brozek, M. Dincă, *Lattice-imposed geometry in metal–organic frameworks: lacunary Zn4O clusters in MOF-5 serve as tripodal chelating ligands for $Ni^{2+}$*, Chem. Sci. 3 (6) (2012) 2110–2113.
[89] J.A. Botas, G. Calleja, M. Sánchez-Sánchez, M.G. Orcajo, Cobalt doping of the MOF-5 framework and its effect on gas-adsorption properties, Langmuir 26 (8) (2010) 5300–5303.
[90] M. Dincă, A. Dailly, Y. Liu, C.M. Brown, D.A. Neumann, J.R. Long, Hydrogen storage in a microporous Metal−Organic framework with exposed Mn2+ coordination sites, J. Am. Chem. Soc. 128 (51) (2006) 16876–16883.
[91] Z.R. Herm, B.M. Wiers, J.A. Mason, J.M. van Baten, M.R. Hudson, P. Zajdel, C.M. Brown, N. Masciocchi, R. Krishna, J.R. Long, Separation of hexane isomers in a metal-organic framework with triangular channels, Science 340 (6135) (2013) 960–964.
[92] H.R. Abid, H. Tian, H.-M. Ang, M.O. Tade, C.E. Buckley, S. Wang, Nanosize Zr-metal organic framework (UiO-66) for hydrogen and carbon dioxide storage, Chem. Eng. J. 187 (2012) 415–420.
[93] M. Kalaj, M.R. Momeni, K.C. Bentz, K.S. Barcus, J.M. Palomba, F. Paesani, S.M. Cohen, Halogen bonding in UiO-66 frameworks promotes superior chemical warfare agent simulant degradation, Chem. Commun. 55 (24) (2019) 3481–3484.
[94] H.R. Abid, J. Shang, H.-M. Ang, S. Wang, Amino-functionalized Zr-MOF nanoparticles for adsorption of CO2 and CH4, International Journal of Smart and Nano Materials 4 (1) (2013) 72–82.
[95] Z.H. Rada, H.R. Abid, H. Sun, J. Shang, J. Li, Y. He, S. Liu, S. Wang, *Effects of -$NO_2$* and -$NH_2$ functional groups in mixed-linker Zr-based MOFs on gas adsorption of $CO_2$ and $CH_4$, Prog. Nat. Sci.: Mater. Int. 28 (2) (2018) 160–167.
[96] A.M. Rasero-Almansa, M. Iglesias, F. Sánchez, Synthesis of bimetallic Zr(Ti)-naphthalendicarboxylate MOFs and their properties as Lewis acid catalysis, RSC Adv. 6 (108) (2016) 106790–106797.
[97] Y. Liu, J.-H. Her, A. Dailly, A.J. Ramirez-Cuesta, D.A. Neumann, C.M. Brown, Reversible structural transition in MIL-53 with large temperature hysteresis, J. Am. Chem. Soc. 130 (35) (2008) 11813–11818.
[98] H.R. Abid, Z.H. Rada, L. Liu, S. Wang, S. Liu, *S*triking $CO_2$ capture and $CO_2/N_2$ separation by Mn/Al bimetallic MIL-53, Polyhedron 193 (2021), 114898.
[99] H.R. Abid, Z.H. Rada, X. Duan, H. Sun, S. Wang, *Enhanced $CO_2$* Adsorption and Selectivity of $CO_2/N_2$ on amino-MIL-53(Al) Synthesized by polar Co-solvents, Energy & Fuels 32 (4) (2018) 4502–4510.
[100] C. Healy, K.M. Patil, B.H. Wilson, L. Hermanspahn, N.C. Harvey-Reid, B.I. Howard, C. Kleinjan, J. Kolien, F. Payet, S.G. Telfer, P.E. Kruger, T.D. Bennett, The thermal stability of metal-organic frameworks, Coord. Chem. Rev. 419 (2020), 213388.
[101] H.U. Escobar-Hernandez, L.M. Pérez, P. Hu, F.A. Soto, M.I. Papadaki, H.-C. Zhou, Q. Wang, Thermal stability of metal–organic frameworks (MOFs): concept, determination, and model prediction using computational chemistry and machine learning, Ind. Eng. Chem. Res. 61 (17) (2022) 5853–5862.
[102] M. Ding, X. Cai, H.-L. Jiang, Improving MOF stability: approaches and applications, Chem. Sci. 10 (44) (2019) 10209–10230.
[103] H.N. Abdelhamid, A.P. Mathew, Cellulose–metal organic frameworks (CelloMOFs) hybrid materials and their multifaceted Applications: a review, Coord. Chem. Rev. 451 (2022), 214263.
[104] T.E. Webber, S.P. Desai, R.L. Combs, S. Bingham, C.C. Lu, R.L. Penn, Size control of the MOF NU-1000 through manipulation of the modulator/linker competition, Cryst. Growth Des. 20 (5) (2020) 2965–2972.
[105] O.K. Farha, I. Eryazici, N.C. Jeong, B.G. Hauser, C.E. Wilmer, A.A. Sarjeant, R.Q. Snurr, S.T. Nguyen, A. Yazaydın, J.T. Hupp, Metal-organic framework materials with ultrahigh surface areas: is the sky the limit? J. Am. Chem. Soc. 134 (36) (2012) 15016–15021.
[106] H. Furukawa, N. Ko, Y.B. Go, N. Aratani, S.B. Choi, E. Choi, A.Ö. Yazaydin, R.Q. Snurr, M. O'Keeffe, J. Kim, Ultrahigh porosity in metal-organic frameworks, Science 329 (5990) (2010) 424–428.
[107] H.K. Chae, D.Y. Siberio-Pérez, J. Kim, Y. Go, M. Eddaoudi, A.J. Matzger, M. O'Keeffe, O.M. Yaghi, D. Materials, G. Discovery, A route to high surface area, porosity and inclusion of large molecules in crystals, Nature 427 (6974) (2004) 523–527.
[108] C.-S. Tsao, M.-S. Yu, T.-Y. Chung, H.-C. Wu, C.-Y. Wang, K.-S. Chang, H.-L. Chen, Characterization of pore structure in Metal−Organic framework by small-angle X-ray scattering, J. Am. Chem. Soc. 129 (51) (2007) 15997–16004.
[109] N. Jiang, Z. Deng, S. Liu, C. Tang, G. Wang, Synthesis of metal organic framework (MOF-5) with high selectivity for CO2/N2 separation in flue gas by maximum water concentration approach, Kor. J. Chem. Eng. 33 (9) (2016) 2747–2755.
[110] Z. Su, Y.-R. Miao, G. Zhang, J.T. Miller, K.S. Suslick, Bond breakage under pressure in a metal organic framework, Chem. Sci. 8 (12) (2017) 8004–8011.
[111] Z.H. Rada, H.R. Abid, J. Shang, H. Sun, Y. He, P. Webley, S. Liu, S. Wang, *Functionalized UiO-66 by Single and binary $(OH)_2$* and $NO_2$ Groups for Uptake of $CO_2$ and $CH_4$, Ind. Eng. Chem. Res. 55 (29) (2016) 7924–7932.
[112] M. Al Haydar, H.R. Abid, B. Sunderland, S. Wang, Multimetal organic frameworks as drug carriers: aceclofenac as a drug candidate, Drug Des. Dev. Ther. 13 (2018) 23–35.
[113] T. Wang, X. Li, W. Dai, Y. Fang, H. Huang, Enhanced adsorption of dibenzothiophene with zinc/copper-based metal–organic frameworks, J. Mater. Chem. A 3 (42) (2015) 21044–21050.
[114] M.R. Azhar, H.R. Abid, H. Sun, V. Periasamy, M.O. Tadé, S. Wang, Excellent performance of copper based metal organic framework in adsorptive removal of toxic sulfonamide antibiotics from wastewater, J. Colloid Interface Sci. 478 (2016) 344–352.
[115] T.V.N. Thi, C.L. Luu, T.C. Hoang, T. Nguyen, T.H. Bui, P.H.D. Nguyen, T.P.P. Thi, *Synthesis of MOF-199 and application to $CO_2$* adsorption, Adv. Nat. Sci. Nanosci. Nanotechnol. 4 (3) (2013), 035016.
[116] C.G. Sonwane, S.K. Bhatia, Characterization of pore size distributions of mesoporous materials from adsorption isotherms, J. Phys. Chem. B 104 (39) (2000) 9099–9110.

[117] S. Storck, H. Bretinger, W.F. Maier, Characterization of micro-and mesoporous solids by physisorption methods and pore-size analysis, Appl. Catal. Gen. 174 (1–2) (1998) 137–146.
[118] M. Thommes, K. Kaneko, A.V. Neimark, J.P. Olivier, F. Rodriguez-Reinoso, J. Rouquerol, K.S. Sing, Physisorption of gases, with special reference to the evaluation of surface area and pore size distribution (IUPAC Technical Report), Pure Appl. Chem. 87 (9–10) (2015) 1051–1069.
[119] Z. Li, D. Pei, R. Tian, C. Lu, Screening the specific surface area for metal-organic frameworks by cataluminescence, Chemosensors 11 (5) (2023) 292.
[120] M. Thommes, Physical adsorption characterization of nanoporous materials, Chem. Ing. Tech. 82 (7) (2010) 1059–1073.
[121] J. Francisco, K.A.C. Sotomayor, Matthias Thommes, Characterization of micro/mesoporous Materials by physisorption: Concepts and case studies, Acc. Mater. Surf. Res. 3 (2) (2018) 34–50.
[122] O.K. Farha, I. Eryazici, N.C. Jeong, B.G. Hauser, C.E. Wilmer, A.A. Sarjeant, R.Q. Snurr, S.T. Nguyen, A.Ö. Yazaydın, J.T. Hupp, Metal–organic framework materials with ultrahigh surface areas: is the sky the limit? J. Am. Chem. Soc. 134 (36) (2012) 15016–15021.
[123] Y. Yang, P. Shukla, S. Wang, V. Rudolph, X.-M. Chen, Z. Zhu, Significant improvement of surface area and CO2 adsorption of Cu–BTC via solvent exchange activation, RSC Adv. 3 (38) (2013).
[124] H.R. Abid, A. Hanif, A. Keshavarz, J. Shang, S. Iglauer, *$CO_2$, $CH_4$, and $H_2$* adsorption Performance of the metal–organic framework HKUST-1 by modified synthesis strategies, Energy & Fuels 37 (10) (2023) 7260–7267.
[125] P.G. Mezey, Functional groups in quantum chemistry, in: P.-O. Löwdin, J.R. Sabin, M.C. Zerner (Eds.), Advances in Quantum Chemistry, Academic Press, 1996, pp. 163–222.
[126] R. Xie, Y. Jin, Y. Chen, W. Jiang, The importance of surface functional groups in the adsorption of copper onto walnut shell derived activated carbon, Water Sci. Technol. 76 (11) (2017) 3022–3034.
[127] P.V. Dau, K.K. Tanabe, S.M. Cohen, Functional group effects on metal–organic framework topology, Chem. Commun. 48 (75) (2012) 9370–9372.
[128] Z.H. Rada, H.R. Abid, H. Sun, S. Wang, *Bifunctionalized metal organic frameworks, UiO-66-NO2-N (N = -NH2, -$(OH)_2$, -$(COOH)_2$), for enhanced Adsorption and Selectivity of $CO_2$* and $N_2$, J. Chem. Eng. Data 60 (7) (2015) 2152–2161.
[129] H.R. Abid, G.H. Pham, H.-M. Ang, M.O. Tade, S. Wang, *Adsorption of $CH_4$* and $CO_2$ on Zr-metal organic frameworks, J. Colloid Interface Sci. 366 (1) (2012) 120–124.
[130] S.C.A. Téllez, E. Hollauer, M.A. Mondragon, V.M. Castaño, Fourier-transform infrared and Raman spectra, vibrational assignment and ab initio calculations of terephthalic acid and related compounds, Spectrochim. Acta Mol. Biomol. Spectrosc. 57 (5) (2001) 993–1007.
[131] S. Bauer, C. Serre, T. Devic, P. Horcajada, J. Marrot, G. Férey, N. Stock, High-throughput assisted rationalization of the formation of metal organic frameworks in the iron(III) aminoterephthalate solvothermal system, Inorg. Chem. 47 (17) (2008) 7568–7576.
[132] N. Iswarya, M.G. Kumar, K. Rajan, J.B.B. Rayappan, Metal organic framework (MOF-5) for sensing of volatile organic compounds, JApSc 12 (16) (2012) 1681–1685.
[133] W.W. Lestari, Irwinsyah, T.E. Saraswati, Y.K. Krisnandi, U.S.F. Arrozi, E. Heraldy, G.T.M. Kadja, Composite material consisting of HKUST-1 and Indonesian activated natural zeolite and its application in CO2 capture, Open Chem. 17 (1) (2019) 1279–1287.
[134] S. Biswas, D.E.P. Vanpoucke, T. Verstraelen, M. Vandichel, S. Couck, K. Leus, Y.-Y. Liu, M. Waroquier, V. Van Speybroeck, J.F.M. Denayer, P. Van Der Voort, *New functionalized metal–organic frameworks MIL-47-X (X = −Cl, −Br, $-CH_3$, $-CF_3$, −OH, $-OCH_3$): synthesis, characterization, and $CO_2$* adsorption properties, J. Phys. Chem. C 117 (44) (2013) 22784–22796.
[135] Q. Liu, L. Ning, S. Zheng, M. Tao, Y. Shi, Y. He, Adsorption of carbon dioxide by MIL-101(Cr): regeneration conditions and influence of flue gas contaminants, Sci. Rep. 3 (1) (2013) 2916.
[136] Y. Feng, J. Yao, Tailoring the structure and function of metal organic framework by chemical etching for diverse applications, Coord. Chem. Rev. 470 (2022), 214699.
[137] L. Figueroa-Quintero, D. Villalgordo-Hernández, J.J. Delgado-Marín, J. Narciso, V.K. Velisoju, P. Castaño, J. Gascón, E.V. Ramos-Fernández, Post-synthetic surface modification of metal–organic frameworks and their potential applications, Small Methods 7 (4) (2023), 2201413.
[138] M.R. Azhar, Y. Arafat, M. Khiadani, S. Wang, Z. Shao, Water-stable MOFs-based core-shell nanostructures for advanced oxidation towards environmental remediation, Compos. B Eng. (2020) 192.
[139] H. Fatima, M.R. Azhar, Y. Zhong, Y. Arafat, M. Khiadani, Z. Shao, Rational design of ZnO-zeolite imidazole hybrid nanoparticles with reduced charge recombination for enhanced photocatalysis, J. Colloid Interface Sci. 614 (2022) 538–546.
[140] Y. Xu, Q. Li, H. Xue, H. Pang, Metal-organic frameworks for direct electrochemical applications, Coord. Chem. Rev. 376 (2018) 292–318.
[141] F. Ambroz, T.J. Macdonald, V. Martis, I.P. Parkin, Evaluation of the BET theory for the characterization of meso and microporous MOFs, Small Methods 2 (11) (2018).